## Title
Whole-brain steady-state CEST at 3 T using MR Multitasking



## Journal
Magnetic Resonance in Medicine, 87(5)

## ISSN
0740-3194

## Authors
Han, Pei
Cheema, Karandeep
Lee, Hsu-Lei
et al.

## Publication Date
2022-05-01

## DOI
10.1002/mrm.29109

Peer reviewed

HHS Public Access

Author manuscript

*Magn Reson Med*. Author manuscript; available in PMC 2022 November 01.

Published in final edited form as:

*Magn Reson Med*. 2022 May ; 87(5): 2363–2371. doi:10.1002/mrm.29109.

# Whole-Brain Steady-State CEST at 3T Using MR Multitasking

**Pei Han, BS**[1,2], **Karandeep Cheema, MS**[1,2], **Hsu-Lei Lee, PhD**[1], **Zhengwei Zhou, PhD**[1], **Tianle Cao, BS**[1,2], **Sen Ma, PhD**[1], **Nan Wang, PhD**[1], **Hui Han, PhD**[1], **Anthony G. Christodoulou, PhD**[*,1,2], **Debiao Li, PhD**[*,1,2]

[1]Biomedical Imaging Research Institute, Cedars-Sinai Medical Center, Los Angeles, CA, United States

[2]Department of Bioengineering, University of California, Los Angeles, CA, United States

## Abstract

**Purpose:** To perform fast 3D steady-state chemical exchange saturation transfer (ss-CEST) imaging using MR Multitasking.

**Methods:** A continuous acquisition sequence with repetitive ss-CEST modules was developed. Each ss-CEST module contains a single-lobe Gaussian saturation pulse, followed by a spoiler gradient and eight FLASH readouts (one “training line” + seven “imaging lines”). 3D Cartesian encoding was used for k-space acquisition. Reconstructed CEST images were quantified with four-pool Lorentzian fitting.

**Results:** Steady-state CEST with whole-brain coverage was performed in 5.6 sec per saturation frequency offset at the spatial resolution of 1.7 × 1.7 × 3.0 $mm^3$. The total scan time was 5.5 min for 55 different frequency offsets. Quantitative CEST maps from multi-pool fitting showed consistent image quality across the volume.

**Conclusion:** 3D steady-state CEST with whole-brain coverage can be done at 3T within 5.5 min using MR Multitasking.

### Keywords

chemical exchange saturation transfer; steady-state CEST; MR Multitasking; APT; rNOE

## 1. Introduction

Chemical exchange saturation transfer (CEST) is a non-contrast MR imaging technique that indirectly detects exchangeable protons in the water pool by pre-saturation at different frequency offsets [1, 2, 3]. CEST MRI provides a novel contrast mechanism to image important physiological information, such as pH and metabolite concentration [4, 5]. It can be applied to detect and diagnose various pathologies, such as cancer [6], ischemia [2, 7], and lymphedema [8].

**Correspondence: Debiao Li, PhD**, Address: Biomedical Imaging Research Institute, Cedars-Sinai Medical Center, 8700 Beverly Blvd. PACT Suite 400, Los Angeles, CA 90048, USA, debiao.li@cshs.org.

*Authors contributed equally to this work

In conventional CEST imaging, each image readout is preceded by a frequency selective saturation module with long enough duration to reach the steady state between the exchanging proton pools and the water pool. Collecting images at different saturation frequency offsets generates the so-called Z-spectrum, which reflects the steady-state signal at sampled frequency offsets for a given saturation power. Wide, symmetric coverage of the Z-spectrum allows multi-pool analysis [9, 10], simultaneously revealing different CEST effects such as amide proton transfer (APT), relayed nuclear Overhauser enhancement (rNOE) effect, and other application-specific effects such as glycoCEST [11], CrCEST [12] and glycoNOE [13]. To achieve a reliable multi-pool analysis, dense sampling of the wide Z-spectrum is generally performed. Given the several dozen frequency offsets typically sampled, the acquisition duration (including the long saturation module) per frequency offset should ideally be limited to a few seconds in order to keep scan times acceptable for clinical practice. This time constraint typically allows only a single-shot k-space acquisition for each frequency offset after the saturation module. This single-shot scheme makes fast, high-quality 3D CEST imaging a challenging technical goal.

One fast approach, the snapshot-CEST method [14], shortened scan times by optimizing the k-space sampling efficiency, such as using spiral-centric reordered k-space acquisition for snapshot gradient-echo (GRE) readout [15, 16] or 3D echo-planar-imaging (EPI) readout with CAIPIRINHA undersampling [17, 18]. It can provide $1.7 \times 1.7$ mm$^2$ in-plane resolution with an FOV of $220 \times 180 \times 54$ mm$^3$ acquired in 7 sec per offset using 3D GRE readout, and 1.8 mm isotropic resolution with and FOV of $256 \times 224 \times 156$ mm$^3$ acquired in 4.3 sec per offset using 3D EPI readout.

A potentially faster approach, the steady-state CEST (ss-CEST) method, performs pre-saturation and k-space sampling in an interleaved pattern with repeated modules [19, 20, 21, 22]. It ensures that the saturation exchange steady state is maintained most of the time within each frequency offset, and the interleaved pattern provides more flexibility in sequence design and possible acceleration. However, initial ss-CEST methods required more than 12 min to acquire the whole Z-spectrum, which is still too long for practical use. Recently, faster ss-CEST was explored in several studies. For instance, a new ss-CEST method combining the radial readout with multilinear singular value decomposition was proposed to further reduce the total scan time to be less than 5 min [23, 24]. Compared with previous ss-CEST approaches, the acquisition time per frequency offset was reduced from more than 10 sec to 7.6 sec [21]; however, the spatial coverage and in-plane resolution was compromised (from $2 \times 2 \times 2$ mm$^3$ with >40 slices to $5 \times 3 \times 3$ mm$^3$ with 15 slices). Another work explored fast 3D ss-CEST using segmented 3D EPI with incoherent undersampling in the $k$-$\omega$ space [25], generating whole-brain 1.8 mm isotropic CEST maps within 4 min.

Compared with EPI acquisition, ss-CEST with GRE acquisition is still slow despite its robustness to off-resonance and distortion. Therefore, we focus on the acceleration of GRE based ss-CEST in this work. In this study, we propose a novel 3D ss-CEST method at 3T using MR Multitasking [26]. MR Multitasking is a low-rank-tensor (LRT) imaging strategy initially developed for quantitative cardiovascular imaging. We extend its application to CEST imaging in this work. With LRT modeling, the correlations among images acquired at

different frequency offsets and among data during the approach to steady-state are exploited to both reduce the scan time and enhance the image quality. This allows the Z-spectrum to be acquired with whole-brain coverage at 1.7 × 1.7 × 3.0 $mm^3$ spatial resolution within 5.5 min.

## 2. Methods

### 2.1 Data acquisition

Fig. 1 illustrates the pulse sequence design and k-space sampling pattern of the proposed Multitasking ss-CEST protocol. The continuous-acquisition pulse sequence consists of repetitive ss-CEST modules. Each ss-CEST module contains a single-lobe Gaussian saturation pulse, followed by a spoiler gradient and eight fast low-angle shot (FLASH) readouts. The module repeated several times at each frequency offset in order to reach steady-state, and then switched to another frequency without any additional delay between modules. K-space lines were sampled using 3D Cartesian encoding. The center line ($k_y = k_z = 0$) was first sampled as "training data", and seven randomized lines with Gaussian distribution in $k_y$ and $k_z$ direction were then sampled as "imaging data" [26].

### 2.2 Image reconstruction

Images from the proposed protocol were represented in form as a 5D image $A(\mathbf{x}, \Delta\omega, \boldsymbol{\tau})$, where $\mathbf{x}$ is the voxel location in three spatial dimensions, $\Delta\omega$ indexes different frequency offsets of saturation pulses, and $\boldsymbol{\tau}$ tracks the time within each frequency offset (indexing the approach to steady-state). The image was reshaped as a three-way tensor $\mathcal{A}$ (grouping together the three spatial dimensions into one mode and assigning $\Delta\omega$ and $\boldsymbol{\tau}$ to the other two modes). Due to high correlation along each dimension, the tensor $\mathcal{A}$ can be modeled as low-rank and thus partially separable [27], e.g.

$$\mathcal{A} = \mathcal{G} \times_1 \mathbf{U}_\mathbf{x} \times_2 \mathbf{U}_{\Delta\omega} \times_3 \mathbf{U}_\tau \tag{1}$$

where $\times_i$ denotes the tensor i-mode product; $\mathbf{U}_\mathbf{x} \in \mathbb{C}^{J \times L_0}$ contains $L_0$ spatial basis functions with $J$ voxels each, $\mathbf{U}_{\Delta\omega} \in \mathbb{C}^{K \times L_1}$ contains $L_1$ basis functions which characterize the Z-spectra, and $\mathbf{U}_\tau \in \mathbb{C}^{M \times L_2}$ contains $L_2$ temporal basis functions which characterize the signal evolution to reach steady-state within each frequency offset; $\mathcal{G} \in \mathbb{C}^{L_0 \times L_1 \times L_2}$ denotes the core tensor. The core tensor and temporal bases can be combined into a temporal factor tensor $\boldsymbol{\Phi} = \mathcal{G} \times_2 \mathbf{U}_{\Delta\omega} \times_3 \mathbf{U}_\tau$, in which case Eq. (1) simplifies to

$$\mathcal{A} = \boldsymbol{\Phi} \times_1 \mathbf{U}_\mathbf{x}\,. \tag{2}$$

Image reconstruction was done similarly to previous MR Multitasking works [28, 29, 30, 31], in two steps:

First, the components of the temporal factor tensor $\boldsymbol{\Phi}$ were estimated from the training data $\mathbf{d}_{\text{tr}}$. Using the known $\Delta\omega$ and $\boldsymbol{\tau}$ indices, all the training data can also be reshaped into a three-way multichannel tensor $\mathcal{D}_{\text{tr}}$ in $(\mathbf{k}, \Delta\omega, \boldsymbol{\tau})$-space, where the first mode comprises

k-space locations **k** from all receiving coils. Then, $\mathcal{G}$, $\mathbf{U}_{\Delta\omega}$, and $\mathbf{U}_{\tau}$ were extracted from the higher-order singular value decomposition (HOSVD) [32] of $\mathcal{D}_{\text{tr}}$.

Second, the spatial basis functions $\mathbf{U}_{\mathbf{x}}$ were determined from the imaging data $\mathbf{d}_{\text{im}}$ by solving the following problem:

$$\widehat{\mathbf{U}}_{\mathbf{x}} = \underset{\mathbf{U}_{\mathbf{x}}}{\operatorname{argmin}} \|\mathbf{d}_{\text{im}} - \Omega(\boldsymbol{\Phi} \times_1 \mathbf{E}\mathbf{U}_{\mathbf{x}})\|_2^2 + \lambda R(\mathbf{U}_{\mathbf{x}}) \tag{3}$$

where **E** is the signal encoding operator, including Fourier transform and coil sensitivity weightings; Ω is the undersampling operator; and $R(\cdot)$ is a regularization functional which was chosen here as a spatial total variation (TV) regularization term in order to additionally exploit compressed sensing.

### 2.3 CEST quantification

After the 5D image tensor **A** was fully reconstructed, a 4D image $\tilde{A}(\mathbf{x}, \Delta\omega)$ was extracted, consisting of the steady-state images at each frequency offset:

$$\tilde{A}(\mathbf{x}, \Delta\omega) = A(\mathbf{x}, \Delta\omega, \tau_{\max}) \tag{4}$$

where $\tau_{\max}$ is the last sampling time point at each frequency offset. $\tilde{A}(\mathbf{x}, \Delta\omega)$ was then used for further CEST analysis for each voxel **x** in the following steps:

1. **Z-spectra generation.** For each voxel $\mathbf{x} = \mathbf{x}_0$, the CEST signal $\tilde{A}(\mathbf{x}_0, \Delta\omega)$ was first normalized with the signal from unsaturated image $S_0(\mathbf{x}_0)$ (acquired at 300 ppm) to generate the Z-spectrum:

$$Z(\mathbf{x}_0, \Delta\omega) = \frac{\tilde{A}(\mathbf{x}_0, \Delta\omega)}{S_0(\mathbf{x}_0)} \tag{5}$$

2. **$B_0$ correction.** The central part of the Z-spectrum (nominal frequency offset $|\Delta\omega| < 1$ppm) was used to determine $\Delta B_0$ with a Lorentzian model [33]. Z-spectra were then shifted for each voxel with corresponding $\Delta B_0$.

3. **Multi-pool Lorentzian fitting** to generate isolated CEST contrasts. The four-pool model was employed, including APT (+3.5 ppm), rNOE (−3.5 ppm), semisolid magnetization transfer (MT, −1.0 ppm), and direct water saturation (DWS, 0 ppm) [9, 17]. The contribution of each pool is represented by a Lorentzian function:

$$L_i(\Delta\omega, A_i, W_i, C_i) = A_i \cdot \frac{W_i^2/4}{W_i^2/4 + (\Delta\omega - C_i)^2} \tag{6}$$

where $\Delta\omega$ is the frequency offset; $A_i$, $W_i$, $C_i$ is the amplitude, width, and center frequency of the i-th Lorentzian curve ($i = 1, 2, 3, 4$). Then, the fitted Z-spectrum can be described as

$$f(\Delta\omega) = 1 - \sum_{i=1}^{4} L_i(\Delta\omega, A_i, W_i, C_i) \quad (7)$$

Eq. (7) was used to fit the Z-spectrum for each voxel using the MATLAB function *lsqnonlin*. The fitting parameters can be found in Supporting Information Table S1.

## 2.4 In vivo experiments

The experiment was approved by the institutional review board of Cedars-Sinai Medical Center. Written informed consent was obtained for all participating subjects. Data were acquired in six (n = 6) healthy volunteers on a 3T MR system (MAGNETOM Vida, Siemens Healthcare, Erlangen, Germany) with a 1Tx/16Rx-channel head/neck coil.

For the proposed Multitasking ss-CEST protocol, CEST parameters were (Fig. 1): TR = 70 ms, saturation pulse duration $t_{sat}$ = 30 ms, saturation pulse flip angle = 500° (effective $B_1$ = 0.93 μT [35]), FA = 5° for FLASH readouts. The module was repeated 80 times at each frequency offset (5.6 sec in total), and then switched to another frequency without delay. Other parameters were: FOV = 220 × 220 × 120 $mm^3$, matrix size = 128 × 128 × 40, spatial resolution = 1.7 × 1.7 × 3.0 $mm^3$. Images of 53 frequency offsets (−100, −40, −30, −20, −15, −10, −9.0, −8.0, −7.0, −6.5, −6.0, −5.5, −5.0, −4.5, −4.0, −3.5, −3.0, −2.5, −2.0, −1.5, −1.0, −0.8, −0.6, −0.4, −0.2, −0.1, 0, 0.1, 0.2, 0.4, 0.6, 0.8, 1.0, 1.5, 2.0, 2.5, 3.0, 3.5, 4.0, 4.5, 5.0, 5.5, 6.0, 6.5, 7.0, 8.0, 9.0, 10, 15, 20, 30, 40, 100 ppm) were acquired from upfield to downfield, with two prolonged unsaturated acquisition $S_0$ (300 ppm) at the beginning and the end. The total imaging time was 5 min 30 s.

Single-slice single-shot FLASH CEST images were acquired as a reference. The frequency offsets were sampled as in ss-CEST. A train of 30 Gaussian pulses of $t_{sat}$ = 30 ms (duty cycle = 50%) and flip angle = 500° were used for saturation. Other parameters were: slice thickness = 10 mm, TR/FA = 3000 ms/5°, 2 averages. The total imaging time was 5 min 54 s for one slice.

T1w images were also acquired with the same image center, FOV, and slice thickness with the 3D ss-CEST protocol for gray matter (GM) and white matter (WM) segmentation.

To test the intra-session repeatability of the protocol, the same Multitasking ss-CEST sequence were performed twice at the same location in four (n = 4) volunteers.

## 2.5 Image analysis

All image reconstruction and image processing were performed with MATLAB R2018a (MathWorks, Natick, Massachusetts, USA) on a Linux workstation with two 2.7-GHz 12-core Intel Xeon CPUs, one NVIDIA Quadro K6000 GPU, and 256 GB RAM.

CEST quantification was done for both 3D Multitasking ss-CEST images and 2D single-shot FLASH CEST images as described in previous sections. Segmented WM and GM in the central slice were selected as regions of interest (ROIs) for statistical analysis. WM/GM segmentation was performed with FSL [36] upon T1w images. The mean values of APT,

rNOE, and MT maps of each subject within GM and WM regions were compared between the proposed 3D Multitasking ss-CEST method and 2D single-shot FLASH CEST method. Statistical graphs were generated with GraphPad Prism 8 (GraphPad Software, La Jolla, California, USA).

## 3. Results

Representative Z-spectra between −15 ppm and 15 ppm are shown in Fig. 2A, B for WM and GM respectively. It can be clearly seen in the figure that the MT effect was more significant in WM than in GM, which is consistent with previous studies [15, 17].

Fig. 3 shows representative (A) $B_0$ estimation result, (B) MT map, (C) rNOE map, and (D) APT maps of the proposed Multitasking ss-CEST method from one healthy volunteer. The image quality was consistent among different slices. Fig. 4 shows the comparison between rNOE, APT, and MT maps generated from the proposed Multitasking ss-CEST method and the 2D single-shot FLASH CEST method. While the fitted rNOE, APT and MT values were generally consistent with each other (also see Fig. 5), maps from the proposed method were less noisy than those from the reference 2D single-shot FLASH method.

Statistics of mean Lorentzian amplitudes within WM and GM regions among different volunteers are presented in Fig. 5. As shown in Fig. 5A, the mean amplitude was consistent among healthy subjects. Contrast ratios of WM:GM for rNOE, APT and MT amplitudes were 1.12, 1.07 and 1.31 from the proposed Multitasking ss-CEST method, near to the reference values of 1.13, 0.94, and 1.35 from the 2D single-shot FLASH CEST method. Note that although the saturation powers were the same, the established “steady state” at data acquisition were different between the proposed method and the reference method (steady state vs. pseudo steady state [22]), which may contribute to the difference in fitted rNOE, APT, MT amplitudes and corresponding WM/GM contrast ratios. The mean values of fitted rNOE, APT and MT amplitudes in WM and GM regions for each volunteer are shown in Supporting Information Fig. S1.

The intra-session repeatability results for each of the three volunteers are displayed in Supporting Information Fig. S2. The Coefficient of Variation (CoV) of rNOE, APT, and MT (considering the values in both GM and WM) were 5.1%, 8.9%, and 9.2% [37].

## 4. Discussion

We developed a novel 3D steady-state CEST method with whole-brain coverage using MR Multitasking. 3D Images of 55 different frequency offsets (including unsaturated ones) were acquired within 5.5 min covering an FOV of 220 × 220 × 120 $mm^3$ at a spatial resolution of 1.7 × 1.7 × 3.0 $mm^3$. The time to acquire the data for each frequency offset was 5.6 seconds. It is more time efficient than previous GRE based methods considering the spatial coverage and the spatial resolution [14, 15, 38].

In contrast to the single-shot acquisition method (or the pseudo-steady-state method) [22], the ss-CEST method ensures that the steady state of the chemical exchanging process is maintained during most of the acquisition time. It allows continuous acquisition for more

efficient traversal of k-space than the single-shot method. Nonetheless, the only additional source of acceleration in the original ss-CEST implementation was limited to parallel imaging.

Low-rankness in spatiospectral signals has been exploited in previous work such as the SPICE method [39] and the Multilinear Singular Value Decomposition (MLSVD) method [24]. In SPICE, the spectroscopic image is modeled as a low-rank matrix to accelerate image acquisition. It was designed for spectroscopic imaging but has not been explored for CEST imaging. The MLSVD method performs post-processing denoising of CEST images by enforcing low-rankness of individual spatial dimensions versus a frequency offset dimension. In contrast, the low-rank tensor model in MR Multitasking enforces low-rankness of a combined spatial dimension (thereby imposing no assumption on spatial structure) versus two individual sequence parameter dimensions: frequency offset and time since frequency increment. Furthermore, Multitasking imposes this model during image reconstruction to accelerate acquisition. In addition to accelerating the acquisition, the Multitasking ss-CEST method has two additional advantages: (1) the approach to the steady state at each frequency offset is modeled and the signal before the steady state is excluded, allowing uncorrupted steady-state values to be used for quantification; (2) the Z-spectra are automatically denoised with the low-rank constraint. Given enough spatiotemporal correlation, the only explicit limiting factor of acceleration becomes the time required to reach steady state at each frequency offset.

In this work, 53 different frequency offsets were sampled between −100 ppm and 100 ppm. In fact, though all the data were reconstructed jointly, not all the frequency offsets were needed in the multi-pool fitting process. The quantitative CEST maps reported in this paper were fitted using only the data from −20 ppm to 20 ppm (after $B_0$ correction). However, those outer frequency offsets, even not used for fitting, are still important in this protocol. Note that the frequency offset is switched from one to another without water signal recovery during the continuous scan. Generally, the time to reach the steady state is shorter if the gap between two adjacent sampling frequency offsets is closer. Therefore, outer frequency offsets (e.g., ±30, ±40, and ±100 ppm) were sampled to “bridge the gap” between unsaturated images and saturated images, so that the steady state could be reached quickly at the following frequency offset [20].

Certain inhomogeneities are present in APT images (Fig. 3D), correlated to $B_0$ inhomogeneities in Fig. 3A. There is possibility of either incomplete $B_0$ correction or incorrect modeling of $B_0$ inhomogeneities in the low-rank model. A locally low-rank approach [40] may model the effects of smooth $B_0$ inhomogeneity more efficiently, which will be explored in future work. Furthermore, the use of advanced active shimming coils may potentially provide better $B_0$ shimming to reduce $B_0$ inhomogeneity during image acquisition [41, 42].

$B_1$ correction [43, 44] was not performed in this feasibility study. This may increase the variability of the CEST quantification results within the same tissue. Therefore, the influence of $B_1$ inhomogeneity on the reliability of quantitative CEST maps needs to be evaluated before exploring the clinical applications of the proposed technique.

A 4-pool Lorentzian fitting method was used to quantify the CEST effects, as in Mueller et al. [17]. Different fitting methods have been used previously, such as the Lorentzian difference (LD) method [15, 45, 46] or the PLOF method [23, 47]. Moreover, a different number of pools were fitted in the studies. Therefore, a standard fitting method which is generally accepted is still not established. Also, in previous works at 3T, different $B_1$ values were chosen. Some representative effective $B_1$ were 0.6 μT [15], 0.65 μT [17], 0.76 μT [23], and a peak $B_1$ of 2 μT was used in several studies [25, 48]. In this work, we use a Gaussian saturation pulse with flip angle = 500° (peak $B_1$ = 2.15 μT, effective $B_1$ = 0.93 μT), which is slightly higher to balance the SNR of the spatial subspace images in MR Multitasking reconstruction and the visibility of the CEST effect in the Z-spectra. Both the choice of accurate CEST fitting method and the optimization of $B_1$ are important questions to explore, but are beyond the scope of this work.

There are several potential improvements to explore in the near future. First, advanced k-space sampling trajectories may be exploited. For instance, non-Cartesian trajectories such as spirals have the potential to improve the sampling efficiency and incoherence over Cartesian acquisition, further reducing the scan time and enhancing the image quality. Second, the sampling pattern of specific frequency offsets can be further optimized to reduce the total number of sampled frequencies, so that the total scan time may be reduced while maintaining the reliability and robustness of the multi-pool fitting. Also, given that the sampling pattern of one “training line” every 70 ms resembles self-gated acquisition used for MR Multitasking in the heart and abdomen, the current ss-CEST protocol has the potential to also be applied to moving organs, such as free-breathing abdominal CEST.

## 5. Conclusion

Three-dimensional steady-state CEST with whole-brain coverage can be done at 3T with a total scan time of 5.5 min and a spatial resolution of 1.7 × 1.7 × 3.0 $mm^3$ using MR Multitasking. Repeatable APT and rNOE maps were generated using the proposed method. This method has the potential to enable fast and high-quality 3D CEST imaging at clinical field strength.

## Supplementary Material

Refer to Web version on PubMed Central for supplementary material.

## Acknowledgements

This work was supported in part by NIH R01 EB028146 and R01 AR066517. Drs. Anthony G. Christodoulou and Debiao Li contributed equally to this work.

## References

1. Ward KM, Aletras AH, Balaban RS. A new class of contrast agents for MRI based on proton chemical exchange dependent saturation transfer (CEST). Journal of magnetic resonance. 2000 Mar 1;143(1):79–87. [PubMed: 10698648]
2. Zhou J, Payen JF, Wilson DA, Traystman RJ, van Zijl PC. Using the amide proton signals of intracellular proteins and peptides to detect pH effects in MRI. Nature medicine. 2003 Aug;9(8):1085–90.

3. Van Zijl PC, Yadav NN. Chemical exchange saturation transfer (CEST): what is in a name and what isn't?. Magnetic resonance in medicine. 2011 Apr;65(4):927–48. [PubMed: 21337419]
4. Vinogradov E, Sherry AD, Lenkinski RE. CEST: from basic principles to applications, challenges and opportunities. Journal of magnetic resonance. 2013 Apr 1;229:155–72. [PubMed: 23273841]
5. Jones KM, Pollard AC, Pagel MD. Clinical applications of chemical exchange saturation transfer (CEST) MRI. Journal of Magnetic Resonance Imaging. 2018 Jan;47(1):11–27. [PubMed: 28792646]
6. Jones CK, Schlosser MJ, Van Zijl PC, Pomper MG, Golay X, Zhou J. Amide proton transfer imaging of human brain tumors at 3T. Magnetic resonance in medicine. 2006 Sep;56(3):585–92. [PubMed: 16892186]
7. Longo DL, Cutrin JC, Michelotti F, Irrera P, Aime S. Noninvasive evaluation of renal pH homeostasis after ischemia reperfusion injury by CEST-MRI. NMR in Biomedicine. 2017 Jul;30(7):e3720.
8. Donahue MJ, Donahue PC, Rane S, Thompson CR, Strother MK, Scott AO, Smith SA. Assessment of lymphatic impairment and interstitial protein accumulation in patients with breast cancer treatment-related lymphedema using CEST MRI. Magnetic resonance in medicine. 2016 Jan;75(1):345–55. [PubMed: 25752499]
9. Zaiss M, Schmitt B, Bachert P. Quantitative separation of CEST effect from magnetization transfer and spillover effects by Lorentzian-line-fit analysis of z-spectra. Journal of magnetic resonance. 2011 Aug 1;211(2):149–55. [PubMed: 21641247]
10. Heo HY, Zhang Y, Lee DH, Hong X, Zhou J. Quantitative assessment of amide proton transfer (APT) and nuclear overhauser enhancement (NOE) imaging with extrapolated semi-solid magnetization transfer reference (EMR) signals: application to a rat glioma model at 4.7 Tesla. Magnetic resonance in medicine. 2016 Jan;75(1):137–49. [PubMed: 25753614]
11. Van Zijl PC, Jones CK, Ren J, Malloy CR, Sherry AD. MRI detection of glycogen in vivo by using chemical exchange saturation transfer imaging (glycoCEST). Proceedings of the National Academy of Sciences. 2007 Mar 13;104(11):4359–64.
12. Haris M, Nanga RP, Singh A, Cai K, Kogan F, Hariharan H, Reddy R. Exchange rates of creatine kinase metabolites: feasibility of imaging creatine by chemical exchange saturation transfer MRI. NMR in Biomedicine. 2012 Nov;25(11):1305–9. [PubMed: 22431193]
13. Zhou Y, van Zijl PC, Xu X, Xu J, Li Y, Chen L, Yadav NN. Magnetic resonance imaging of glycogen using its magnetic coupling with water. Proceedings of the National Academy of Sciences. 2020 Feb 11;117(6):3144–9.
14. Zaiss M, Ehses P, Scheffler K. Snapshot-CEST: optimizing spiral-centric-reordered gradient echo acquisition for fast and robust 3D CEST MRI at 9.4 T. NMR in Biomedicine. 2018 Apr;31(4):e3879. [PubMed: 29372571]
15. Deshmane A, Zaiss M, Lindig T, Herz K, Schuppert M, Gandhi C, Bender B, Ernemann U, Scheffler K. 3D gradient echo snapshot CEST MRI with low power saturation for human studies at 3T. Magnetic resonance in medicine. 2019 Apr;81(4):2412–23. [PubMed: 30431179]
16. Haase A Snapshot FLASH MRI. Applications to T1, T2, and chemical-shift imaging. Magnetic resonance in medicine. 1990 Jan;13(1):77–89. [PubMed: 2319937]
17. Mueller S, Stirnberg R, Akbey S, Ehses P, Scheffler K, Stöcker T, Zaiss M. Whole brain snapshot CEST at 3T using 3D-EPI: Aiming for speed, volume, and homogeneity. Magnetic resonance in medicine. 2020 Nov;84(5):2469–83. [PubMed: 32385888]
18. Breuer FA, Blaimer M, Heidemann RM, Mueller MF, Griswold MA, Jakob PM. Controlled aliasing in parallel imaging results in higher acceleration (CAIPIRINHA) for multi-slice imaging. Magnetic resonance in medicine. 2005 Mar;53(3):684–91. [PubMed: 15723404]
19. Jones CK, Polders D, Hua J, Zhu H, Hoogduin HJ, Zhou J, Luijten P, Van Zijl PC. In vivo three-dimensional whole-brain pulsed steady-state chemical exchange saturation transfer at 7 T. Magnetic resonance in medicine. 2012 Jun;67(6):1579–89. [PubMed: 22083645]
20. Jones CK, Huang A, Xu J, Edden RA, Schär M, Hua J, Oskolkov N, Zacà D, Zhou J, McMahon MT, Pillai JJ. Nuclear Overhauser enhancement (NOE) imaging in the human brain at 7 T. Neuroimage. 2013 Aug 15;77:114–24. [PubMed: 23567889]

21. Heo HY, Jones CK, Hua J, Yadav N, Agarwal S, Zhou J, van Zijl PC, Pillai JJ. Whole-brain amide proton transfer (APT) and nuclear Overhauser enhancement (NOE) imaging in glioma patients using low-power steady-state pulsed chemical exchange saturation transfer (CEST) imaging at 7T. Journal of Magnetic Resonance Imaging. 2016 Jul;44(1):41–50. [PubMed: 26663561]
22. Khlebnikov V, Geades N, Klomp DW, Hoogduin H, Gowland P, Mougin O. Comparison of pulsed three-dimensional CEST acquisition schemes at 7 tesla: steady state versus pseudosteady state. Magnetic resonance in medicine. 2017 Jun;77(6):2280–7. [PubMed: 27455028]
23. Sui R, Chen L, Li Y, Huang J, Chan KW, Xu X, van Zijl PC, Xu J. Whole-brain amide CEST imaging at 3T with a steady-state radial MRI acquisition. Magnetic resonance in medicine. 2021 Aug;86(2):893–906. [PubMed: 33772859]
24. Chen L, Cao S, Koehler RC, van Zijl PC, Xu J. High-sensitivity CEST mapping using a spatiotemporal correlation-enhanced method. Magnetic resonance in medicine. 2020 Dec;84(6):3342–50. [PubMed: 32597519]
25. Lee H, Choi SH, Sohn CH, Kim SG, Lee J, Park J. Rapid three-dimensional steady-state chemical exchange saturation transfer magnetic resonance imaging. Magnetic resonance in medicine. 2021 Mar;85(3):1209–21. [PubMed: 32851659]
26. Christodoulou AG, Shaw JL, Nguyen C, Yang Q, Xie Y, Wang N, Li D. Magnetic resonance multitasking for motion-resolved quantitative cardiovascular imaging. Nature Biomedical Engineering. 2018 Apr;2(4):215–226.
27. Liang ZP. Spatiotemporal imaging with partially separable functions. In Biomedical Imaging: From Nano to Macro, 2007. ISBI 2007. 4th IEEE International Symposium on 2007 Apr 12 (pp. 988–991). IEEE.
28. Han P, Zhang R, Wagner S, Xie Y, Cingolani E, Marban E, Christodoulou AG, Li D. Electrocardiogram-less, free-breathing myocardial extracellular volume fraction mapping in small animals at high heart rates using motion-resolved cardiovascular magnetic resonance multitasking: a feasibility study in a heart failure with preserved ejection fraction rat model. Journal of Cardiovascular Magnetic Resonance. 2021 Feb;23(8):1–11. [PubMed: 33390185]
29. Ma S, Wang N, Fan Z, Kaisey M, Sicotte NL, Christodoulou AG, Li D. Three-dimensional whole-brain simultaneous T1, T2, and T1ρ quantification using MR Multitasking: Method and initial clinical experience in tissue characterization of multiple sclerosis. Magnetic resonance in medicine. 2021 Apr;85(4):1938–52. [PubMed: 33107126]
30. Ma S, Nguyen CT, Han F, Wang N, Deng Z, Binesh N, Moser FG, Christodoulou AG, Li D. Three-dimensional simultaneous brain T1, T2, and ADC mapping with MR Multitasking. Magnetic resonance in medicine. 2020 Jul;84(1):72–88. [PubMed: 31765496]
31. Wang N, Xie Y, Fan Z, Ma S, Saouaf R, Guo Y, Shiao SL, Christodoulou AG, Li D. Five-dimensional quantitative low-dose Multitasking dynamic contrast-enhanced MRI: Preliminary study on breast cancer. Magnetic resonance in medicine. 2021 Jun;85(6):3096–111. [PubMed: 33427334]
32. De Lathauwer L, De Moor B, Vandewalle J. A multilinear singular value decomposition. SIAM journal on Matrix Analysis and Applications. 2000;21(4):1253–78.
33. Kim M, Gillen J, Landman BA, Zhou J, Van Zijl PC. Water saturation shift referencing (WASSR) for chemical exchange saturation transfer (CEST) experiments. Magnetic resonance in medicine. 2009 Jun;61(6):1441–50. [PubMed: 19358232]
34. Haris M, Singh A, Cai K, Kogan F, McGarvey J, DeBrosse C, Zsido GA, Witschey WR, Koomalsingh K, Pilla JJ, Chirinos JA. A technique for in vivo mapping of myocardial creatine kinase metabolism. Nature medicine. 2014 Feb;20(2):209–14.
35. Zu Z, Li K, Janve VA, Does MD, Gochberg DF. Optimizing pulsed-chemical exchange saturation transfer imaging sequences. Magnetic resonance in medicine. 2011 Oct;66(4):1100–8. [PubMed: 21432903]
36. Jenkinson M, Beckmann CF, Behrens TE, Woolrich MW, Smith SM. Fsl. Neuroimage. 2012 Aug 15;62(2):782–90. [PubMed: 21979382]
37. Synek V Evaluation of the standard deviation from duplicate results. Accreditation and quality assurance. 2008 Jun;13(6):335–7.

38. Krishnamoorthy G, Nanga RP, Bagga P, Hariharan H, Reddy R. High quality three-dimensional gagCEST imaging of in vivo human knee cartilage at 7 Tesla. Magnetic resonance in medicine. 2017 May;77(5):1866–73. [PubMed: 27174078]

39. Lam F, Liang ZP. A subspace approach to high-resolution spectroscopic imaging. Magnetic resonance in medicine. 2014 Apr;71(4):1349–57. [PubMed: 24496655]

40. Zhang T, Pauly JM, Levesque IR. Accelerating parameter mapping with a locally low rank constraint. Magnetic resonance in medicine. 2015 Feb;73(2):655–61. [PubMed: 24500817]

41. Han H, Song AW, Truong TK. Integrated parallel reception, excitation, and shimming (iPRES). Magnetic resonance in medicine. 2013 Jul;70(1):241–7. [PubMed: 23629974]

42. Cai Y, Yang H, Li X, Hu T, Huang Y, Shan Y, Lu M, Liu WS, Li D, Han H. Optimization of Multi-Coil Array Design for Efficient Human Brain Shimming at 3T. In Proceedings of the 28th Annual Meeting of ISMRM 2020 (p. 4229).

43. Windschuh J, Zaiss M, Meissner JE, Paech D, Radbruch A, Ladd ME, Bachert P. Correction of B1-inhomogeneities for relaxation-compensated CEST imaging at 7 T. NMR in biomedicine. 2015 May;28(5):529–37. [PubMed: 25788155]

44. Schuenke P, Windschuh J, Roeloffs V, Ladd ME, Bachert P, Zaiss M. Simultaneous mapping of water shift and B1 (WASABI)—Application to field-inhomogeneity correction of CEST MRI data. Magnetic resonance in medicine. 2017 Feb;77(2):571–80. [PubMed: 26857219]

45. Goerke S, Soehngen Y, Deshmane A, Zaiss M, Breitling J, Boyd PS, Herz K, Zimmermann F, Klika KD, Schlemmer HP, Paech D. Relaxation-compensated APT and rNOE CEST-MRI of human brain tumors at 3 T. Magnetic resonance in medicine. 2019 Aug;82(2):622–32. [PubMed: 30927313]

46. Akbey S, Ehses P, Stirnberg R, Zaiss M, Stöcker T. Whole-brain snapshot CEST imaging at 7 T using 3D-EPI. Magnetic resonance in medicine. 2019 Nov;82(5):1741–52. [PubMed: 31199016]

47. Chen L, Barker PB, Weiss RG, van Zijl PC, Xu J. Creatine and phosphocreatine mapping of mouse skeletal muscle by a polynomial and Lorentzian line-shape fitting CEST method. Magnetic resonance in medicine. 2019 Jan;81(1):69–78. [PubMed: 30246265]

48. Heo HY, Zhang Y, Jiang S, Lee DH, Zhou J. Quantitative assessment of amide proton transfer (APT) and nuclear overhauser enhancement (NOE) imaging with extrapolated semisolid magnetization transfer reference (EMR) signals: II. Comparison of three EMR models and application to human brain glioma at 3 Tesla. Magnetic resonance in medicine. 2016 Apr;75(4):1630–9. [PubMed: 26033553]

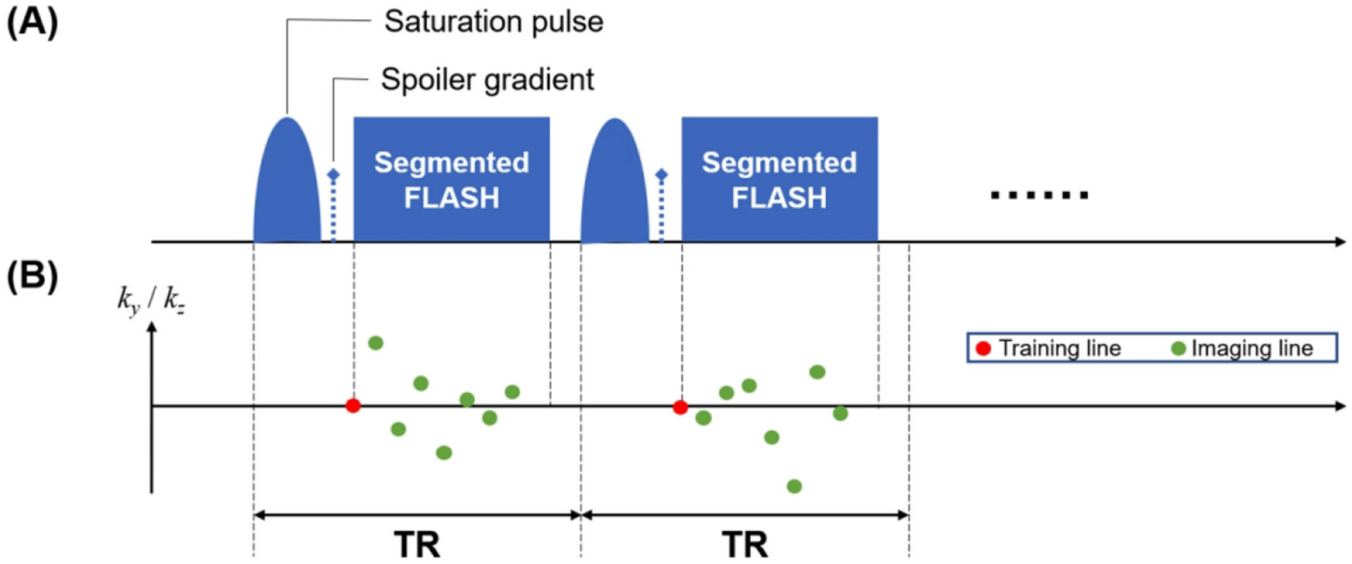


**Figure 1:**

**(A) Sequence design:** Each module (TR = 70ms) contains a single-lobe Gaussian saturation pulse ($t_{sat}$ = 30ms, flip angle = 500°), followed by a spoiler gradient and 8 FLASH readout lines (1 training line + 7 imaging lines, flip angle = 5°). The module repeated at a specific frequency offset ($N_{rep}$ = 80) and then switched to another. **(B) k-space sampling pattern:** In each module, the "training line" (center k-space line) is first acquired, followed by seven "imaging lines" (pseudo-randomly sampled lines with Gaussian distribution in $k_y$ and $k_z$directions).

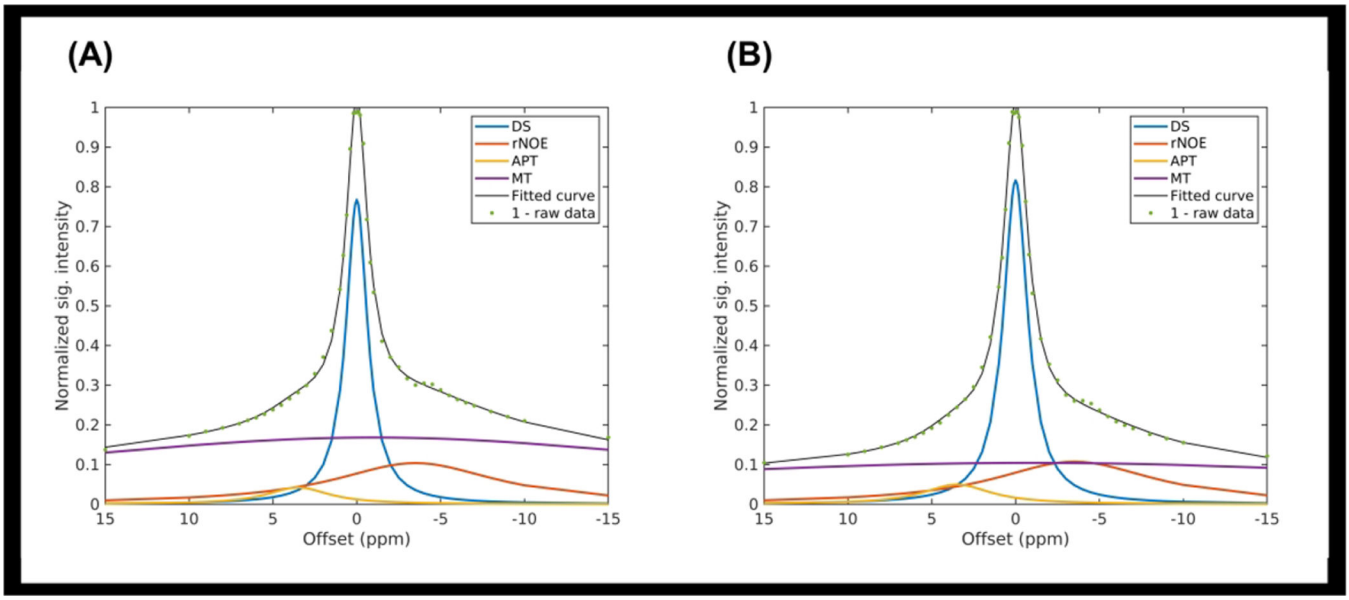


**Figure 2:**

Representative Z-spectra from **(A)** the white matter (WM) region and **(B)** the grey matter (GM) region of a healthy volunteer. For convenience, raw data (the green dots in the figure) were plotted as $1 - Z(\Delta\omega)$.

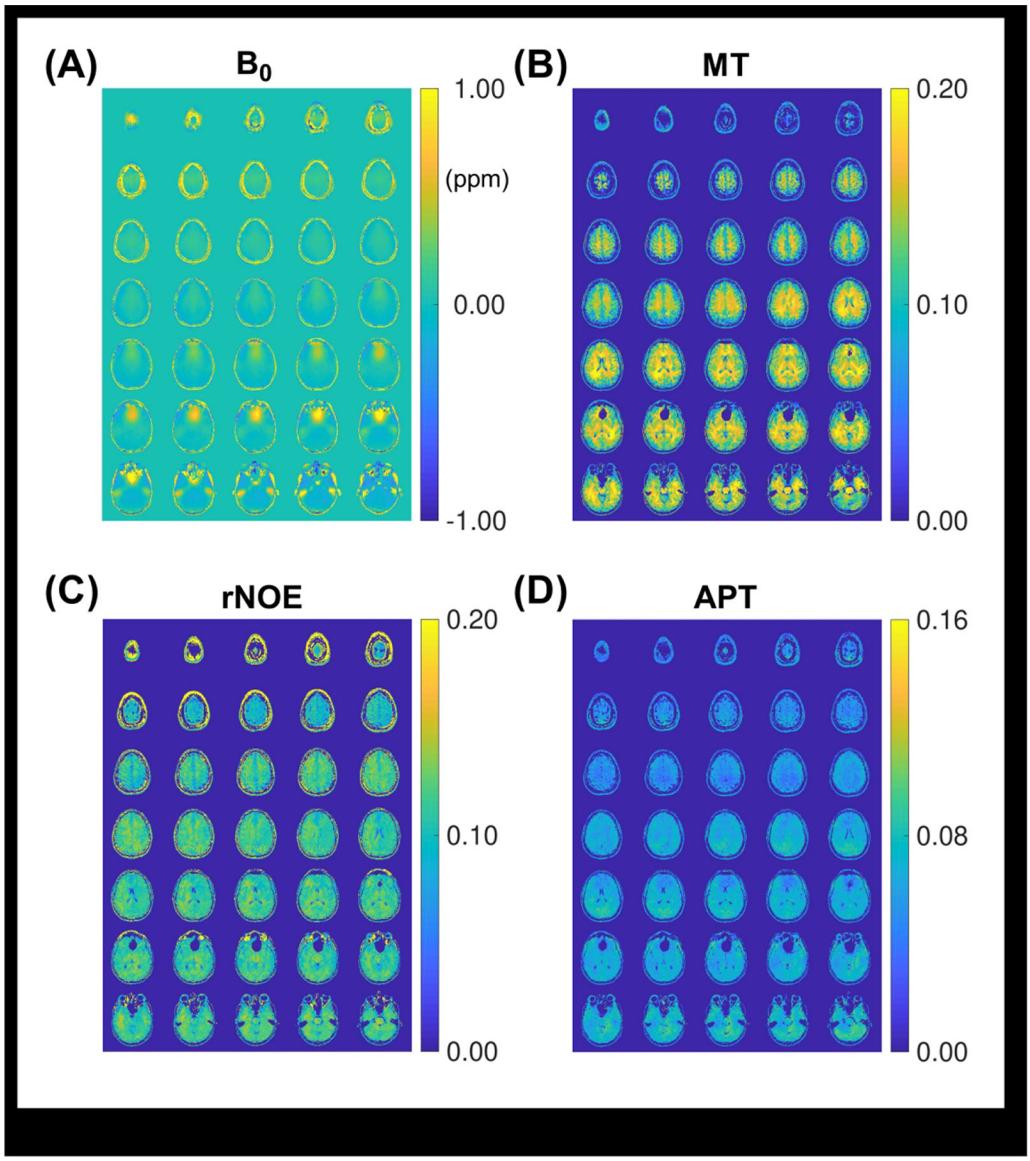


**Figure 3:**

**(A-D)** Representative $B_0$ estimation results and MT, rNOE, APT maps of the proposed Multitasking ss-CEST method (From A to D: $B_0$, MT, rNOE, APT). 35 out of 40 slices are presented here. The outermost 5 slices are discarded for display because the aliasing at the boundary makes the fitting result less reliable.

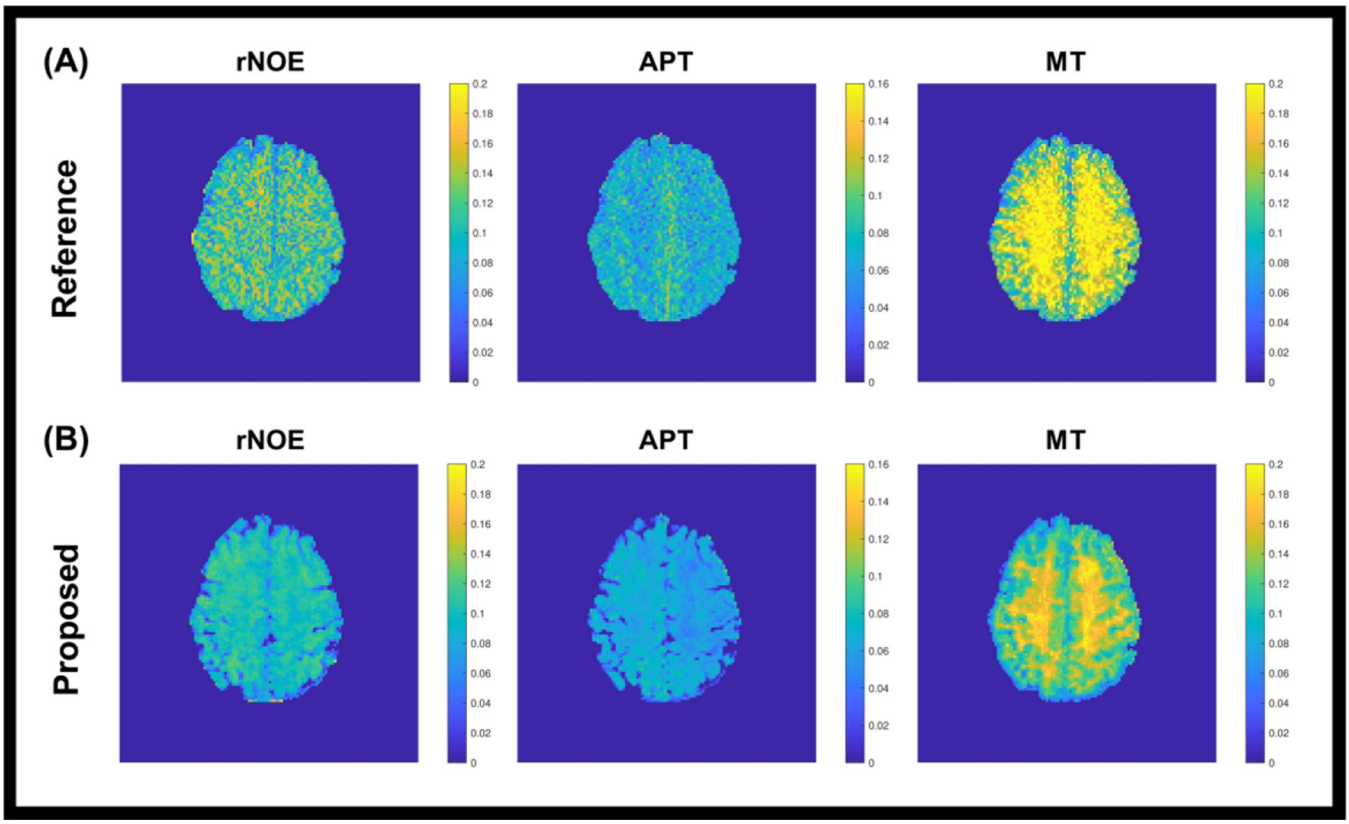


**Figure 4:**

Comparison between maps generated from **(A)** the 2D single-shot FLASH method and **(B)** the proposed Multitasking ss-CEST method. Note that the slice thickness of 10mm used in the 2D single-shot FLASH CEST method was larger than 3mm in the proposed 3D Multitasking ss-CEST method. Therefore, though the center of the slice matched between (A) and (B), the spatial coverages were not completely the same.

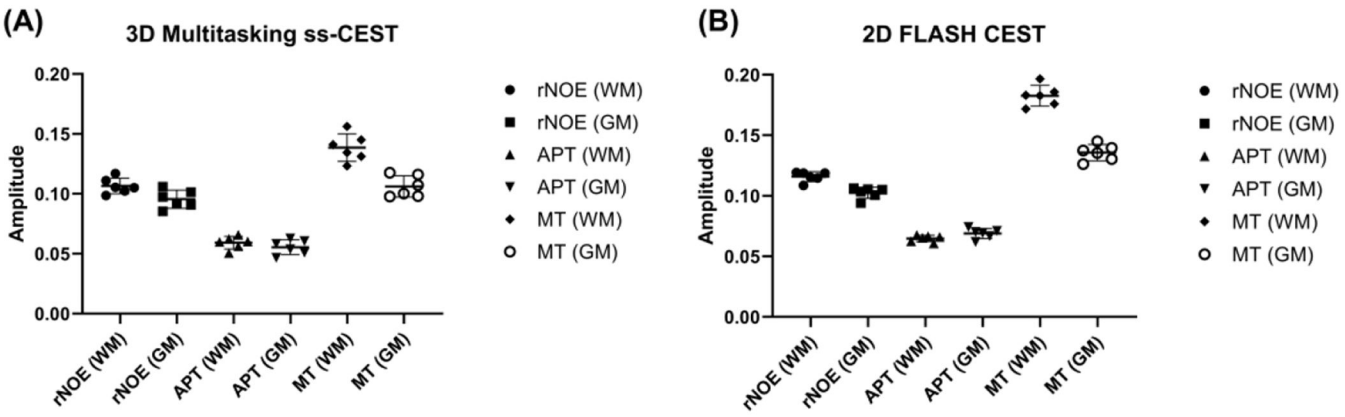


(C)

| | rNOE | | APT | | MT | |
|---|---|---|---|---|---|---|
| (All in %) | WM | GM | WM | GM | WM | GM |
| Multitasking ss-CEST | 10.66 ± 0.65 | 9.55 ± 0.76 | 5.92 ± 0.53 | 5.55 ± 0.62 | 13.86 ± 1.15 | 10.62 ± 0.89 |
| Single-shot FLASH CEST | 11.59 ± 0.41 | 10.25 ± 0.46 | 6.48 ± 0.26 | 6.89 ± 0.42 | 18.26 ± 0.85 | 13.57 ± 0.67 |

**Figure 5:**

Average Lorentzian amplitudes within WM and GM regions among different volunteers. The mean amplitude is consistent among healthy subjects with **(A)** the proposed method and **(B)** the reference method. **(C)** Contrast ratios of WM:GM for rNOE/APT/MT: 1.12/1.07/1.31 (Multitasking ss-CEST) vs. 1.13/0.94/1.35 (2D single-shot FLASH CEST).